Volume 1 | Number 1 | Jan 2013 | Pages 1–100

Nanoscale

www.rsc.org/nanoscale

ARTICLE TYPE

Ultra-high capacitance hematite thin films with controlled nanoscopic morphologies

Jingling Liu,[a] Eunjik Lee,[a] Yong-Tae Kim[a] and Young-Uk Kwon*,[a,b]

We synthesized α-Fe$_2$O$_3$ (hematite) thin films with two different nanoscopic morphologies through self-assembly between a Fe-precursor and a Pluronic tri-block copolymer (F127) followed by aging and calcination. Relative humidity (RH) during the aging step of the spin-coated films was found to be critical in determining the morphologies. A network structure of nanowires ~6 nm in diameter formed when the

10 RH was 75%. The resulting nanowire hematite thin film (NW) had 150-250 nm-sized macropores. When the RH was 0%, mesoporous hematite thin film (MP) with a wormlike pore structure and pore size of ~9 nm formed. Investigation of the electrochemical properties of these films revealed that they had very high specific capacitances of 365.7 and 283.2 F/g for NW and MP, respectively, at a current density of 3 A/g in a 0.5 M Na$_2$SO$_3$ electrolyte. Both of these capacitance values are considerably higher than those

15 previously reported for hematite-based electrodes. We attributed this to the high porosity of the thin films, which enables ready access of electrolyte ions to the electrode surfaces, and their ultra-thin size, comparable to that of the depletion layer, allowing the low conductivity of hematite to be overcome. The higher capacitance of NW than MP is likely due to the accelerated electron transport through the crystalline nanowires in NW.

Introduction

20 Recently, enormous efforts have been made to develop energy storage devices with high power and high energy density along with long-cycle life to meet increasing demands of consumer electronics.[1-3] Supercapacitors are an attractive solution because of their unique combination of high power and high energy

25 densities.[4-6] Depending on the charge storage mechanism, supercapacitors are classified into two types: electric double layer capacitors (EDLC) and pseudocapacitors.[7-9] In an EDLC, energy storage results from the accumulation of electronic or ionic charges at the interface between the electrode and electrolyte; the

30 cyclic voltammetry (CV) curve is rectangular in shape, and the capacitance is normally independent of scan rate. In contrast, in a pseudocapacitor, energy storage arises from a reversible faradaic reaction of the electrode material; the CV curve shows redox peaks and the capacitance normally decreases with an increase in

35 scan rate. Various metal oxides such as RuO$_2$, IrO$_2$, NiO, CoO$_x$, SnO$_2$, and MnO$_2$ have been investigated as electrode materials, and some of these have very high specific capacitances.[10-15] However, most of these materials have drawbacks, such as high

40 toxicity, high cost, or limited availability, hindering their use in commercial applications.

Among metal oxides, iron oxides are considered as promising materials for supercapacitor electrodes due to their environmental friendliness, fairly low cost, and abundance.[16-21] Until recently,

45 the focus has mainly been on Fe$_3$O$_4$ due to its high conductivity

($\sim10^2$-10^3 S/cm).[22] Fe$_3$O$_4$, however, has the disadvantages of low stability under ambient conditions, demanding synthesis conditions to ensure phase purity, and difficulty in controlling morphologies. In contrast, α-Fe$_2$O$_3$ (hematite) has attracted far

50 less attention mainly because of its much lower conductivity ($\sim10^{-14}$ S/cm) than that of Fe$_3$O$_4$.[22] However, because hematite has several important advantages, such as high stability and facile synthesis with easy control of phase purity and morphology over Fe$_3$O$_4$, it would be highly desirable to develop electrode materials

55 based on hematite.

In order to address the low conductivity problem of hematite, it is often blended with carbon-based materials, particularly graphene sheets. Such an approach, however, raises other issues. Graphene sheets have a tendency to restack or agglomerate,

60 thereby reducing electrolyte ion access.[22, 23] Control of morphology also becomes increasingly more difficult as the number of components increases. Most importantly, carbon-modified hematite is only available in powder form, and adhesion to the current collector is often a serious problem. Therefore,

65 electrodes based on binder-free films are optimal for the development of high-performance supercapacitor electrodes.

Specific capacitance is highly dependent on morphology and surface area.[4, 24, 25] In the case of hematite, its low conductivity makes control of morphology at the mesoscopic or nanoscopic

70 level particularly important.[26-29] For this reason, hematite-based materials with various morphologies for supercapacitors have been synthesized, such as nanowires, nanotubes, nanoporous materials, nanosheets, nanoparticles, and hierarchical structures.[17,

[24, 25] Nanoporous materials have been emphasized because these materials have a large surface area, which increases intercalation and deintercalation of electrolytes species,[25] and 1D structures such as nanowires and nanotubes are deemed to be beneficial for electron transfer. Recently, hierarchical structures have been pursued to obtain the benefits of different morphologies.[7, 24]

Because of its low conductivity, the depletion layer within hematite tends to be very thin, on the order of a few nm. However, almost all hematite nanoscopic morphologies reported in the literature are much larger than 10 nm.[17, 24, 25] Therefore, to develop efficient hematite-based electrodes, the ability to synthesize feature sizes on a sub-10 nm scale is essential.

In the present work, we synthesized hematite thin films with nanoscopic morphologies by exploiting self-assembly between a structure-directing surfactant polymer and an iron oxide precursor. As numerous papers on mesoporous materials have demonstrated, this approach can produce nanoscopic morphologies with feature sizes smaller than 10 nm. We found that a simple change in a single synthesis parameter, namely the humidity level during aging of the films, induced a remarkable change in morphology, resulting in the production of two distinct nanoscopic-structured thin films. Mesoporous hematite film with a pore size of ~9 nm and wall thickness of ~5 nm (hereafter MP) was obtained, as was a novel network structure of ~6 nm nanowires with macropores (NW). Electrochemical analyses revealed that both MP and NW electrodes had unprecedented electrochemical capacitance, part of which can be attributed to their sub-10 nm feature sizes. Details are reported below.

2. Experimental Section

2.1. Fabrication of NW and MP electrodes

MP and NW samples were prepared by spin-casting a precursor solution followed by aging to induce self-assembly and calcination. We described the synthesis of MP in our previous paper.[30] The synthesis of NW was almost identical except for one synthesis parameter, the humidity during the aging step. Briefly, 1 g of $Fe(NO_3)_3 \cdot 9H_2O$ was dissolved in 5 mL anhydrous ethanol, followed by stirring for 5 h at 40 °C; this was accompanied by a color change from yellow red to deep red, indicative of generation of iron oxide hydroxide species.[31] 400 mg of Pluronic triblock copolymer F127 $((EO)_{106}(PO)_{70}(EO)_{107}$, EO = ethylene oxide, PO = propylene oxide) was added to the nanoparticle solution, with subsequent stirring for 2 h. The coating solution was spin-coated onto fluorine-doped tin oxide (FTO) substrate at 5000 rpm for 30 s under a controlled relative humidity (RH) of 70% at 24 – 26 °C. For the MP samples, coated films were placed in an 80 °C oven under 0% RH for 2 days. For the NW samples, coated films were placed in a homemade chamber with 75% RH, which was also placed in an oven at 80 °C for 2 days. The RH of 75% was maintained by placing a saturated solution of NaCl in the chamber. Finally, the aged MP and NW samples were heated at 400 °C at a ramping rate of 1 °C/min for 2 h to fully remove surfactant.

Amounts of hematite in MP and NW samples were measured by mass changes before and after the removal of hematite by etching with a HF solution. Five samples of each type were prepared and used to obtain these measurements. Averaged masses for both MP and NW were the same at 40 ±1 μg/cm^2; this

was expected because the procedures used to prepare the two types of samples were exactly the same except for aging conditions.

2.2. Characterization

Morphologies were observed via field emission scanning electron microscopy (FE-SEM, JEOL JSM – 7401F) and field emission high-resolution transmission electron microscopy (FE-TEM, JEM-2100F). Raman spectra were recorded using the 514 nm line of an Ar^+ laser (Renishaw, inVia). Water contact angles of MP and NW surfaces were obtained using a Theta Optical Tensiometer (KSV instruments, Ltd.) with a digital camera connected to a computer. For TEM and Raman measurements, samples were scraped off from the FTO substrates. Chemical bonding and oxidation states of MP and NW samples were investigated by X-ray photoelectron spectroscopy (XPS, Perkin-Elmer PHI 660). Specific surface areas of MP and NW were estimated by evaluating the adsorption of various concentrations of N719 dye molecules. MP and NW samples were immersed in ethanol solutions of N719 at various concentrations for 24 h. Amount of dye adsorption was calculated as the difference in UV-Vis absorption (UV-3600 Shimadzu spectrophotometer) peak intensity of the dye solution (λ = 520 nm) before and after adsorption. Adsorption data were fitted to the Langmuir binding equation to calculate the maximum theoretical binding amount of dye.[32] By using the known geometric data on N719,[33] the surface areas of MP and NW were calculated to be 114 and 368 m^2/g, respectively (ESI Fig. S2 and S3).

2.3. Electrochemical measurements

CV curves were recorded using a potentiostat/galvanostat station (Ivium Compactstat) in a three-electrode system. An aqueous 0.5 M Na_2SO_3 solution was employed as the electrolyte, while an Ag/AgCl (saturated KCl) electrode and a Pt-net were used as the reference and counter-electrode, respectively. Galvanostatic charge–discharge studies were performed using a WonA Tech potentiostat/galvanostatic instrument (WPG10). Electrochemical impedance spectroscopy (EIS) measurements were performed in a 0.5 M Na_2SO_3 aqueous electrolyte solution with an amplitude of 10 mV and frequency variation from 100 KHz to 10 mHz at 0 V vs. Ag/AgCl. The impedance parameters were obtained from least-squares fits to an equivalent circuit by using a commercial program (ZMAN).

3. Results and Discussion

3.1 Morphological and structural characterization

In this study, thin films of hematite with two different types of nanoscopic morphologies were synthesized and their capacitive properties were compared. The two morphologies were achieved through self-assembly between nanoparticles of iron oxide hydroxide species and F-127 surfactant, followed by calcination. It is noteworthy that the two distinct nanoscopic morphologies of NW and MP were obtained under exactly the same synthesis conditions; the only difference was the RH during aging. Elucidation of the formation mechanisms of these morphologies will require in-depth studies of the evolution of self-assembly structures as a function of composition and other synthesis parameters, which is not possible at the present stage. However, it

is well known that self-assembly structures are strongly affected by the volume ratio between two immiscible phases.[34] Apparently, the RH value governs the water content in the film material and, thus, affects the self-assembly structure through variation of the volume ratio.

Morphological details of MP were provided in our previous study.[30] As shown in Fig. 1, MP has ~9 nm sized pores and ~5 nm thick walls, and high-resolution TEM (HRTEM) image (inset of Fig. 1b) reveals that the walls have lattice fringes with d values of 0.27 and 0.25 nm, which correspond to the (104) and (110) planes of hematite, respectively.
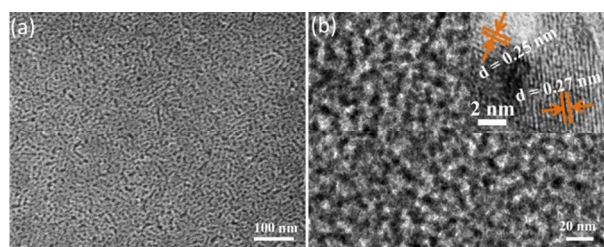

Fig. 1 Electron microscopy images on MP: (a) SEM and (b) TEM images. Inset in (b) is a HRTEM image showing the lattice fringes of the wall material.
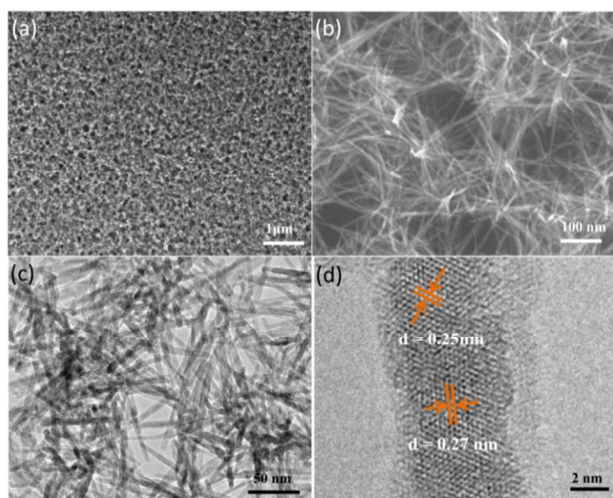

Fig.2 Electron microscopy images on NW: (a) Low and (b) high magnification of SEM images, (c) TEM and (d) HRTEM images.

SEM and TEM images of NW are shown in Fig. 2. SEM images taken at different magnifications (Fig. 2a and 2b) and the low magnification TEM image in Fig. 2c show a network of nanowires ~6 nm in diameter with macropores of 150-250 nm between the nanowires. The HRTEM image (Fig. 2d) shows the lattice fringes of a nanowire with d values of 0.27 and 0.25 nm, which correspond to the (104) and (110) planes of hematite, respectively. Although there are a few precedents of 1D nanostructures of hematite, all of them have dimensions much larger than 10 nm.[17, 24, 25] The smallest reported size of hematite we found in the literature was nanotubes with a wall thickness of ~20 nm.[24] Those authors attributed the enhanced capacitive performance (138 $F \cdot g^{-1}$ at a current density of 1.3 $A \cdot g^{-1}$) to the extremely high surface area and the ability to provide short highways for ion and electron transfer. Generation of ~6 nm thick

hematite nanowires therefore holds great promise for further enhancement of capacitive performance.

Phase identity of MP and NW as hematite was confirmed by Raman spectroscopy (Fig. 3). Spectra of the two samples were almost identical with peaks at 213, 276, 389, 481, and 582 cm^{-1}. These peaks match well with the characteristic Raman peaks of hematite. Other iron oxide phases, such as magnetite and goethite, have completely different spectral patterns that are easy to distinguish from hematite (Fig. 3).[35, 36] Highly crystalline hematite has been reported to show peaks at 225 (A_{1g}), 245 (E_g), 292 (E_g), 411 (E_g), 496 (A_{1g}), and 610 (E_g) cm^{-1} due to transverse optical modes.[17, 35, 36] Compared with these reference peaks, the peaks of our samples were broader and red-shifted, which is likely due to the smaller crystallite size of our samples.[35, 36] It is well-known that nanomaterials (smaller than 20 nm) show red-shifts of optical phonon modes. This phenomenon is explained with the Phonon Confinement Model (PCM) according to which the magnitude of the red-shift increases as the feature size decreases.[37] The almost same Raman peak positions of MP and NW are probably because the dimensions of pore walls of MP and the diameter of NW are close to each other. In case of iron oxide nanoparticles, the red-shift is related with the weakening of Fe-O bonds in the FeO_6 octahedra.[36] The power of the source beam also affects the peak position and shape through the heating of samples during the measurement. Since the power of our measurement (2.6 mW) is higher than in the references on bulk hematite (0.8 mW), this factor also may contribute to the red-shift of peaks.[38]

We also attempted to record X-ray diffraction (XRD) patterns of our samples. However, the very small quantities of hematite (40 µg per one sample for a typical synthesis) precluded the possibility of obtaining quality XRD patterns for definitive phase identification. Notwithstanding, the lattice fringes from the HRTEM images and the Raman spectroscopy data were sufficient to ascertain that both MP and NW were composed of hematite. In addition, the XPS data (ESI Fig. S1) indicated that the Fe species were all Fe^{3+} without a trace of Fe^{2+}, suggesting that iron species were all incorporated in the hematite phase.
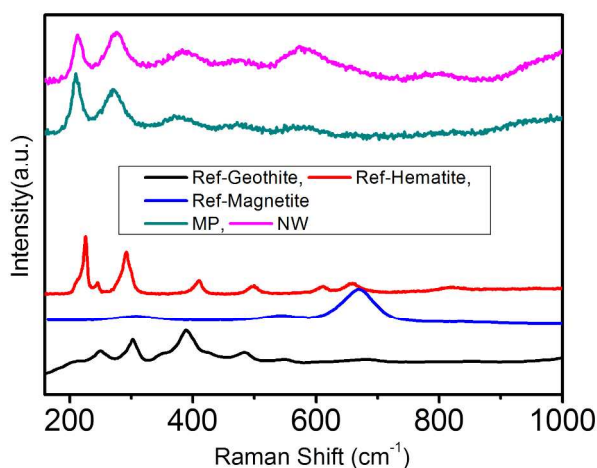

Fig. 3 Raman spectra of MP and NW samples, and reference spectra of goethite, magnetite, and hematite from the RRUFF database. (The RRUFFID is R120086 for goethite, R080025 for magnetite, and R050300.2 for hematite, respectively)

3.2 Effect of morphology on the physical properties of hematite films

We studied the consequences of the different morphologies of MP and NW on surface area by measuring adsorption isotherms of a dye, hydrophilicity/hydrophobicity by measuring contact angles, and electrical properties by using EIS.

Surface area is a critical determinant of the performance of a material, especially for electrode applications. Unfortunately, however, due to the very small quantities of sample that we had available, we could not measure surface area using the conventional N_2 adsorption method. We therefore devised a method based on the adsorption of N719 molecules to estimate surface area. A number of papers have related the amount of dye adsorbed to surface area.[33] By applying the Langmuir binding model to our adsorption data, we calculated the maximum amounts of N719 molecules on the two types of hematite films. By using the known geometry of N719, the surface areas were calculated to be 114 m^2/g for MP and 368 m^2/g for NW (ESI Figs. S2 and S3). Because the theoretical surface areas based on the simplified corresponding models were 78 and 127 m^2/g, respectively, we felt that our measured values were unrealistically large. We suspect that adsorption of dye molecules does not conform to the monolayer model. Rather, the dye molecules may form multiple layers, probably because the interaction of N719 with hematite is not as strong as with titania as in typical dye-sensitized solar cells. If multiple layer adsorption takes place, the amount of adsorption in MP is bound to be limited by the pore dimension while NW does not impose any geometrical limitation, explaining the discrepancy between the model calculations and experimental data. At any rate, both of our theoretical and experimental results indicate that the surface area of NW is considerably larger than that of MP.

Contact angle with water is a direct and effective way to measure the wetting properties of a solid surface, which is influenced by many physical and chemical factors such as surface roughness, chemical heterogeneity, as well as hydrophilicity/hydrophobicity.[39, 40] Despite the contribution of several factors to the contact angle, we measured it to extract useful information regarding the capacitive properties of the hematite films. As expected, both MP and NW had hydrophilic surfaces with contact angles of ~60˚ and ~15˚, respectively (ESI Fig. S4).

We attributed the different contact angles of the two hematite films to the differences in the nature of their interfaces. At the molecular level, the interaction energy between the water molecules and the hematite surface should be the same in both types of films. However, from the perspective of water, the formation of water-hematite interfaces for MP and NW samples could be assimilated by the formation of cavities or droplets in the water-air interface depending on the relative volumes of water and hematite. Because the pore volume of NW was much larger than the volume of nanowires and water would have filled the pores, the nanowires could be considered to occupy cavities in water. In contrast, in the case of MP, because water had to smear into the ~9 nm sized pores, the situation was similar to the formation of water droplets. Because internal pressure is always larger than external pressure across a cavity or droplet interface, the formation of an interface with MP required higher pressure than in bulk water. This situation was reversed in NW. Therefore, we can conclude that wetting of the MP surface requires more energy than wetting of the NW surface, explaining our observations. This may also have implications regarding the structure of water molecules at the interfaces of MP and NW. In the case of MP, the higher pressure necessitates a higher density of water. Therefore, there may be more resistant to diffusion of electrolyte species through the pores in MP than in NW. Of course, other factors such as the formation of an electrical double layer can provide additional resistance to ion diffusion inside pores. However, it is clear that ion diffusion in MP is more difficult than in NW, which may have important consequences for their capacitive properties.

EIS is a powerful tool to study the fundamental behavior of electrode materials, such as their electrical conductivity and ion transfer capacity.[24, 41, 42] Typical Nyquist and Bode plots of MP and NW samples in the frequency range of 100 kHz-10 mHz in a 0.5 M Na_2SO_3 electrolyte solution are shown in Fig. 4. As shown in Fig. 4a, the EIS spectra of MP and NW are almost identical in shape with a semicircle in the high frequency range and a linear line in the low frequency range. Generally, the equivalent circuit of such a plot involves three parameters: sum resistance (R_s), solid electrolyte interphase (SEI) resistance (R_f), and charge transfer resistance (R_{ct}).[24, 41, 42] R_s represents the total resistance of the system, including the inherent resistances of the electrode, the electrolyte and the contact resistance between the electrode and the current collector. It is obtained from the intercept with the real axis in the high frequency region. R_f is the resistance of the surface film formed on the electrodes. R_{ct} is related to double-layer capacitance or pseudocapacitance, and is obtained from the diameter of the semi-circle in the high frequency region. The slope of the linear segment in the low frequency region determines the phase angle ϕ, which is related to diffusion of redox species in the electrolyte. In an ideal supercapacitor, ϕ is close to 90°.[41, 43] The equivalent circuit is shown in the inset of Fig. 4b, and the fitted impedance parameters are listed in Table 1. NW has lower R_s, R_{ct}, and higher ϕ values than MP. However, the SEI layer is influenced not only by chemical properties, but also by surface area, morphology, and the crystallinity of the active materials.[44] Therefore, the difference in R_f between NW and MP is likely due to the differences between these two materials in specific area, morphology, and crystallinity. We attribute the smaller charge transfer resistance of NW than MP to the presence of ultrathin 1D nanowires, as these can smooth and shorten the pathway for charge transfer. The higher phase angle of NW than that of MP may be partly due to the difference in pore size between these two materials. The larger pores of NW would facilitate the mobility of redox species to a greater extent than the smaller pores of MP, resulting in capacitive behaviour closer to the ideal than that of MP. Because numerous factors contribute to sum resistance, it is not obvious which factor contribute the most to the difference in sum resistance between MP and NW. However, the larger pores of NW are expected less resistive than the smaller pores of MP in terms of ionic current flow through pores. In addition, it seems likely that because of the 1D nanowire morphology of NW, NW has fewer grain boundaries than MP for electron conduction.
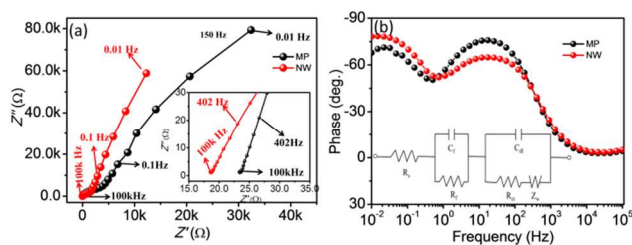
Fig. 4 (a) Nyquist plots and (b) Bode plots of MP and NW electrodes in the frequency range from 10^5 Hz to 10^{-2} Hz at an applied potential of 0 V vs. Ag/AgCl. The inset in (a) shows
5 Nyquist plots at high-frequency region, and the inset in (b) shows the equivalent circuit.

Table 1 Impedance parameters derived from the equivalent circuit for MP and NW samples.

Samples	R_s	R_f (Ω)	R_{ct} (Ω)	ϕ (Degree) at 10^{-2} Hz
MP	23.5	437.8K	3.8K	67
NW	18.4	2.0M	1.7K	78

10

3.3 Capacitance properties

CV data of MP and NW electrodes at different scan rates in a 0.5 M Na_2SO_3 electrolyte solution are shown in Fig. 5. Currents of MP and NW electrodes are proportional to the scan rate, and both
15 CV curves show distorted rectangular shapes with minor redox peaks, distinct from ideal EDLC behavior or ideal pseudocapacitive behavior. The distorted rectangular shapes indicate that the capacitance of MP and NW electrodes may be due to the combination of charge storage in the electric double-
20 layer at the electrode/electrolyte interface and in the host material on the surface through redox reactions.[24, 45, 46] Differences in the shape of the CV curves of the MP and NW electrodes is likely due to different contributions by these two mechanisms. The NW sample has large macropores, favoring diffusion of electrolyte
25 ions and resulting in an increase in active sites where redox reactions can occur.
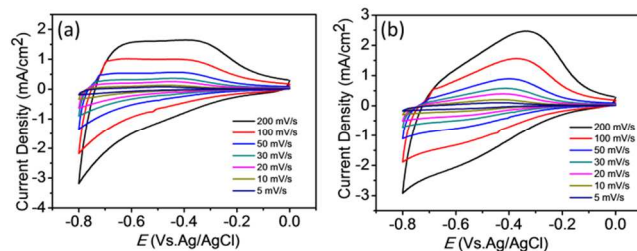

Fig. 5 Cyclic voltammograms of (a) MP and (b) NW electrodes at different scan rates in a 0.5 M Na_2SO_3 electrolyte.

30   Variations in specific capacitances of MP and NW electrodes as a function of scan rate are presented in ESI Fig. S5. At the lowest sweep potential rate of 5 mV/s, the capacitances of MP and NW electrodes were calculated to be 281.2 F/g and 354.3 F/g, respectively. As the scan rate increased, the specific capacitances
35 of both electrodes decreased. This behavior is probably due to

prevention of access of ions to deep pores or inner materials at high scan rates, so that active sites could not be fully utilized for charge storage.[47, 48]
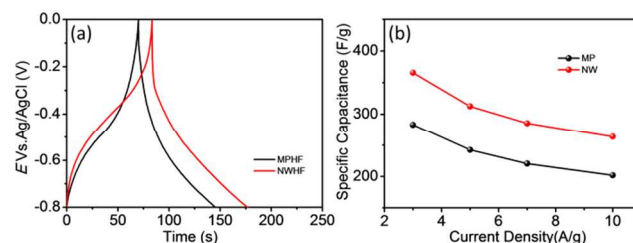

Fig. 6 (a) The first galvanostatic charge-discharge curves of MP
40 and NW electrodes at a current density of 3 A/g. (b) Specific capacitance values of MP and NW electrodes as a function of applied current density.

Galvanostatic charge-discharge curves of MP and NW
45 electrodes at a current density of 3 A/g are shown in Fig. 6a. Specific capacitances were calculated according to the equation:

$$C_{sp} = \frac{I \Delta t}{m \Delta V}$$

where I (mA) is the applied current, Δt (s) is the discharge time, m (mg) is the weight of the active electrode, and ΔV (V) is the potential drop during the discharge.[43] Capacitances were
50 calculated to be 283.2 and 365.7 A/g for MP and NW, respectively; these values agreed well with those from the CV measurements. Curves of specific capacitance as a function of applied current density are presented in Fig. 6b. The capacitance of MP and NW samples decreased with an increase in applied
55 current density due to limited ion accessibility.
Energy density (E) and power density (P) can be calculated by using the following equations.[48, 49]

$$E = \frac{1}{2} C_{sp} \Delta V^2$$

where ΔV is the potential window of discharge process, and

$$P = \frac{E}{\Delta t}$$

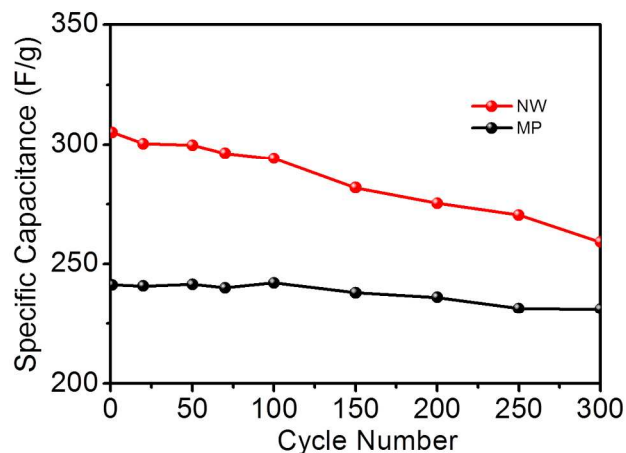where Δt is the discharge time.

60 **Fig. 7** Stability tests of MP and NW electrodes at a current density of 5 A/g.

The energy density and power density of the MP sample are 6.78 Wh/kg and 170 W/kg at 3A/g current density, respectively, while those of the NW sample are 8.12 Wh/kg and 170 W/kg, respectively.

Cycling performance of MP and NW samples was assessed at a constant current density of 5A/g in a 0.5 Na_2SO_3 solution for 300 cycles; results are shown in Fig. 7. There was no apparent attenuation in specific capacitance of MP after 300 cycles. However, the NW sample was less stable than the MP sample. It appears that the thin nanowires did not have sufficient mechanical strength to withstand the stress imposed by cycling.

As mentioned in the introduction, literature on hematite-based supercapacitors is scarce, and most studies on hematite with different morphologies have small capacitances. For instance, Wang's group reported a specific capacitance of 116.25 F/g for mesoporous multi-layer nanosheets with 3 nm pores.[25] A porous flowerlike nanostructure with 6.4 nm pores was reported to have specific capacitance of 127 F/g by Shivakumara's group.[50] Recently, Binitha and colleagues reported a specific capacitance of 256 F/g for porous 1D fibers with a fiber diameter of 700-750 nm and pore dimension of 5.7 nm.[17] These and other recent reports on hematite-based supercapacitors are summarized in ESI Table S1.

Capacitive properties of MP and NW are higher than any of those previously reported for hematite-based electrodes without additional components. Although the capacitance of MP (281 F/g from CV and 283 F/g from galvanostatic data) is smaller than that of NW (354 F/g from CV and 366 F/g from galvanostatic data), it is still considerably large compared with hematite-based reports, probably because MP has larger pores than any of the hematite-based electrodes evaluated previously. Although small pores increase surface area, too small pores may hinder the diffusion of electrolyte inside the pores. In addition, because hematite walls are very thin (~5 nm in thickness), the morphology of MP may be able to make most of the film material participate in the charging-discharging mechanism and, hence, increase the specific capacitance.

The remarkably high capacitance value of NW deserves deeper attention. Its specific capacitance is comparable to or even higher than that of hematite-based electrodes with modifications by incorporation of carbon-based materials or doping foreign elements to overcome its low conductivity. Although further detailed studies are required, the large capacitance of NW is likely due to its large surface area, large pore size, and very thin and crystalline nanowires. Its properties may potentially be further improved by optimizing these aspects. Furthermore, electrodes with very high capacitance properties can potentially be developed by appropriate blending of NW with carbon or other materials. With the beneficial properties of hematite and the facile synthesis method of NW, our results are expected to contribute to the future development of supercapacitors based on hematite and other materials.

4. Conclusions

We synthesized hematite thin films with two different nanoscopic morphologies, namely mesoporous hematite with ~9 nm-sized pores, and a novel network structure of ultrathin nanowires ~6 nm in diameter with macropores of 150-250 nm, through simple self-assembly with control of humidity. These materials are distinguished from related materials in the literature in that their critical morphological characteristics are less than 10 nm in size. Our electrochemical capacitance data revealed that both films had remarkable capacitance properties. MP had a specific capacitance of 283.2 F/g. Its large surface area and pores appeared to enable fast diffusion of electrolyte ions, contributing to its high capacitance. NW had an even higher capacitance than MP of 365.7 F/g, which we attributed to the network structure of crystalline 1D nanowires that favored electron transport, an ultrahigh surface area providing a large number of surface active sites, and macropores for ready access of electrolyte ions for intercalation and deintercalation reactions. Our findings have implications for both the future development of supercapacitors based on hematite and for material design and fabrication methods.

4. Acknowledgment

Notes and references

a SKKU Advanced Institute of Nanotechnology, Sungkyunkwan University, Suwon, 440-746, Republic of Korea
b Department of Chemistry, Sungkyunkwan University, Suwon, 440-746, Republic of Korea Fax: +82 031 290 7075; Tel: +82 031 290 7070; E-mail: ywkwon@skku.edu

† Electronic Supplementary Information (ESI) available: [details of any supplementary information available should be included here]. See DOI: 10.1039/b000000x/

‡ Footnotes should appear here. These might include comments relevant to but not central to the matter under discussion, limited experimental and spectral data, and crystallographic data.

1. J. R. Miller and A. F. Burke, *Electrochem. Soc. Interface*, 2008, **17**, 53.
2. P. Simon and Y. Gogotsi, *Nat Mater*, 2008, **7**, 845.
3. D.-H. Kim, N. Lu, R. Ma, Y.-S. Kim, R.-H. Kim, S. Wang, J. Wu, S. M. Won, H. Tao, A. Islam, K. J. Yu, T.-i. Kim, R. Chowdhury, M. Ying, L. Xu, M. Li, H.-J. Chung, H. Keum, M. McCormick, P. Liu, Y.-W. Zhang, F. G. Omenetto, Y. Huang, T. Coleman and J. A. Rogers, *Science*, 2011, **333**, 838.
4. G. Wang, L. Zhang and J. Zhang, *Chem. Soc. Rev*, 2012, **41**, 797.
5. R. Kötz and M. Carlen, *Electrochim Acta*, 2000, **45**, 2483.
6. M. Winter and R. J. Brodd, *Chem. Rev*, 2004, **104**, 4245.
7. A. G. Pandolfo and A. F. Hollenkamp, *J. Power Sources*, 2006, **157**, 11.
8. A. S. Aricò, P. Bruce, B. Scrosati, J. M. Tarascon and W. Van Schalkwijk, *Nature Mater*, 2005, **4**, 366.
9. A. Burke. *J. Power Sources*, 2000, **91**, 37.
10. J. T. Zhang and X. S. Zhao, *Carbon*, 2013, **52**, 1.
11. H. Kim and B. N. Popov, *J. Power Sources*, 2002, **104**, 52.
12. S. A. Mamuru and K. I. Ozoemena, *Electrochem. Commun*, 2010, **12**, 1539.
13. K. Kuratani, H. Tanaka, T. Takeuchi, N. Takeichi, T. Kiyobayashi and N. Kuriyama, *J. Power Sources*, 2009, **191**, 684.

14. X. Wang, A. Sumboja, E. Khoo, C. Yan and P. S. Lee, *J. Phys. Chem. C,* 2012, **116**, 4930.

15. P. Soudan, J. Gaudet, D. Guay, D. Bélanger and R. Schulz, *Chem. Mater*, 2002, **14**, 1210.

16. X. Zhao, C. Johnston and P. S. Grant, *J. Mater. Chem*, 2009, **19**, 8755.

17. G. Binitha, M. S. Soumya, A. A. Madhavan, P. Praveen, A. Balakrishnan, K. R. V. Subramanian, M. V. Reddy, S. V. Nair, A. S. Nair and N. Sivakumar, *J. Mater. Chem. A*, 2013, **1**, 11698.

18. X. Xia, Q. Hao, W. Lei, W. Wang, D. Sun and X. Wang, *J. Mater. Chem*, 2012, **22**, 16877.

19. W. Yang, Z. Gao, J. Wang, B. Wang and L. Liu, *Solid State Sci*, 2013, **20**, 46.

20. D. Liu, X. Wang, X. Wang, W. Tian, J. Liu, C. Zhi, D. He, Y. Bando and D. Golberg, *J. Mater. Chem. A*, 2013, **1**, 1952.

21. X. Wang, W. Tian, D. Liu, C. Zhi, Y. Bando and D. Golberg, *Nano Energy*, 2013, **2**, 257-267.

22. K. K. Lee, S. Deng, H. M. Fan, S. Mhaisalkar, H. R. Tan, E. S. Tok, K. P. Loh, W. S. Chin and C. H. Sow, *Nanoscale*, 2012, **4**, 2958.

23. C. Liu, Z. Yu, D. Neff, A. Zhamu and B. Z. Jang, *Nano Lett*, 2010, **10**, 4863.

24. K. Xie, J. Li, Y. Lai, W. Lu, Z. A. Zhang, Y. Liu, L. Zhou and H. Huang, *Electrochem. Commun*, 2011, **13**, 657.

25. D. Wang, Q. Wang and T. Wang, *Nanotechnology*, 2011, **22**, 135604.

26. D. Lei, M. Zhang, B. Qu, L. Chen, Y. Wang, E. Zhang, Z. Xu, Q. Li and T. Wang, *Nanoscale*, 2012, **4**, 3422.

27. Q.-q. Xiong, J.-p. Tu, X.-h. Xia, X.-y. Zhao, C.-d. Gu and X.-l. Wang, *Nanoscale*, 2013, **5**, 7906.

28. M. Y. Son, Y. J. Hong, J.-K. Lee and Y. Chan Kang, *Nanoscale*, 2013, **5**, 11592.

29. H. Liu and G. Wang, *J. Mater. Chem. A*, 2014, **2**, 9955.

30. J. Liu, M. Shahid, Y.-S. Ko, E. Kim, T. K. Ahn, J. H. Park and Y.-U. Kwon, *Phys. Chem. Chem. Phys*, 2013, **15**, 9775.

31. R. K. Dani, H. Wang, S. H. Bossmann, G. Wysin and V. Chikan, *J. Chem. Phys*, 2011, **135**, 224502.

32. B. H. Hameed, D. K. Mahmoud and A. L. Ahmad, *J. Hazard. Mater*, 2008, **158**, 65.

33. C. Wang, X. Zhang, Y. Zhang, Y. Jia, B. Yuan, J. Yang, P. Sun and Y. Liu, *Nanoscale*, 2012, **4**, 5023.

34. G. J. d. A. A. Soler-Illia, C. Sanchez, B. Lebeau and J. Patarin, *Chem Rev*, 2002, **102**, 4093-4138.

35. D. L. A. de Faria and F. N. Lopes, *Vib. Spectrosc*, 2007, **45**, 117.

36. I. V. Chernyshova, M. F. Hochella Jr and A. S. Madden, *Phys. Chem. Chem. Phys*, 2007, **9**, 1736.

37. K. W. Adu, Q. Xiong, H. R. Gutierrez, G. Chen and P. C. Eklund, *Appl. Phys. A*, 2006, **85**, 287-297.

38. I. Chourpa, L. Douziech-Eyrolles, L. Ngaboni-Okassa, J.-F. Fouquenet, S. Cohen-Jonathan, M. Soucé, H. Marchais and P. Dubois, *Analyst*, 2005, **130**, 1395.

39. S. Giljean, M. Bigerelle, K. Anselme and H. Haidara, *Appl. Surf. Sci*, 2011, **257**, 9631.

40. V. Khranovskyy, T. Ekblad, R. Yakimova and L. Hultman, *Appl. Surf. Sci*, 2012, **258**, 8146.

41. C. G. Liu, M. Liu, F. Li and H. M. Cheng, *Appl. Phys. Lett*, 2008, **92**, 143108.

42. D. Nandi, A. K. Ghosh, K. Gupta, A. De, P. Sen, A. Duttachowdhury and U. C. Ghosh, *Mater. Res. Bull*, 2012, **47**, 2095.

43. L. Wang, H. Ji, S. Wang, L. Kong, X. Jiang and G. Yang, *Nanoscale*, 2013, **5**, 3793.

44. E. Peled, D. Golodnitsky, A. Ulus and V. Yufit, *Electrochim Acta*, 2004, **50**, 391.

45. M.-S. Wu and R.-H. Lee, *J. Electrochem. Soc*, 2009, **156**, A737.

46. S.-Y. Wang, K.-C. Ho, S.-L. Kuo and N.-L. Wu, *J. Electrochem. Soc*, 2006, **153**, A75.

47. P. M. Kulal, D. P. Dubal, C. D. Lokhande and V. J. Fulari, *J. Alloys Compd*, 2011, **509**, 2567.

48. R. B. Rakhi, W. Chen, D. Cha and H. N. Alshareef, *Nano Lett*, 2012, **12**, 2559.

49. P. M. Hallam, M. Gómez-Mingot, D. K. Kampouris and C. E. Banks, *RSC Adv*, 2012, **2**, 6672.

50. S. Shivakumara, T. R. Penki and N. Munichandraiah, *ECS Electrochem Lett*, 2013, **2**, A60.